Solution structure of the CD3$\varepsilon\delta$ ectodomain and comparison with CD3$\varepsilon\gamma$ as a basis for modeling T cell receptor topology and signaling

Zhen-Yu J. Sun*[†], Sun Taek Kim[†‡], Il Chul Kim[‡§], Amr Fahmy*, Ellis L. Reinherz[‡¶], and Gerhard Wagner*[¶]

*Department of Biological Chemistry and Molecular Pharmacology and [‡]Laboratory of Immunobiology, Departments of Medical Oncology and Medicine, and Dana–Farber Cancer Institute, Harvard Medical School, Boston, MA 02115

Communicated by Alfred G. Redfield, Brandeis University, Waltham, MA, October 13, 2004 (received for review September 10, 2004)

Invariant CD3 subunit dimers (CD3$\varepsilon\gamma$, CD3$\varepsilon\delta$, and CD3$\zeta\zeta$) are the signaling components of the $\alpha\beta$ T cell receptor (TCR). The recently solved structure of murine CD3$\varepsilon\gamma$ revealed a unique side-to-side interface and central β-sheets conjoined between the two C2-set Ig-like ectodomains, with the pairing of the parallel G strands implying a potential concerted piston-type movement for signal transduction. Although CD3γ and CD3δ each dimerize with CD3ε, there are differential CD3 subunit requirements for receptor assembly and signaling among T lineage subpopulations, presumably mandated by structural differences. Here we present the solution structure of the heterodimeric CD3$\varepsilon\delta$ complex. Whereas the CD3ε subunit conformation is virtually identical to that in CD3$\varepsilon\gamma$, the CD3δ ectodomain adopts a C1-set Ig fold, with a narrower GFC front face β-sheet that is more parallel to the ABED back face than those β-sheets in CD3ε and CD3γ. The dimer interface between CD3δ and CD3ε is highly conserved among species and of similar character to that in CD3$\varepsilon\gamma$. Glycosylation sites in CD3δ are arranged such that the glycans may point away from the membrane, consistent with a model of TCR assembly that allows the CD3δ chain to be in close contact with the TCR α-chain. This and many other structural and biological features provide a basis for modeling putative TCR/CD3 extracellular domain associations. The fact that the two clusters of transmembrane helices, namely, the three CD3ε–CD3γ–TCRβ segments and the five CD3ε–CD3δ–TCRα–CD3ζ–CD3ζ segments, are presumably centered beneath the G strand-paired CD3 heterodimers has important implications for TCR signaling.

single-chain C1-Ig fold | immunoreceptor tyrosine-based activation motif | NMR structure | T cell development

The $\alpha\beta$ T cell receptor (TCR) is a multimeric complex composed of an antigen-binding $\alpha\beta$ clonotypic heterodimer and the signal-transducing invariant CD3 subunit dimers CD3$\varepsilon\gamma$, CD3$\varepsilon\delta$, and CD3$\zeta\zeta$ (1–8). Thus, the $\alpha\beta$ TCR complex consists of eight polypeptides (5, 8, 9). Sequence determination and biochemical analyses suggest that each CD3ε, CD3γ, and CD3δ subunit contains an extracellular Ig-like domain, a membrane-proximal stalk region, a transmembrane (TM) helix, and a cytoplasmic tail. The interaction between an $\alpha\beta$ TCR heterodimer and a specific antigenic peptide bound to an MHC molecule (pMHC) initiates a cascade of downstream signaling events via the immunoreceptor tyrosine-based activation motifs (ITAMs) in the cytoplasmic tails of the associated CD3 subunits (10–12). The various CD3 chains interact differentially with intracellular adaptors and signaling molecules, inducing distinct patterns of cellular protein tyrosine phosphorylation upon activation (11, 13–16).

How recognition of pMHC by a clonotypic $\alpha\beta$ heterodimer on the T cell surface evokes intracellular signaling via the adjacent CD3 components remains unknown. However, the solution structure of a heterodimeric murine CD3$\varepsilon\gamma$ complex revealed a unique side-to-side hydrophobic interface with conjoined β-sheets between the two Ig-like ectodomains (C2-set folds[‖]) (17). The rigidity of parallel pairing in their respective C-terminal β-strand elements raised the possibility that concerted piston-type displacement of CD3$\varepsilon\gamma$ upon TCR ligation may be involved in the initiation of T cell signaling (17). Recently, the crystal structure of the human CD3$\varepsilon\gamma$ heterodimer complexed with the Fab fragment of OKT3, a therapeutic mAb, identified a similar architecture (18).

Although the CD3γ and the CD3δ subunits each pair with CD3ε, there are differences in CD3 subunit requirements for various T lineage populations and their developmental stages (2, 19–26). For example, pre-TCR and $\gamma\delta$ TCR functions are impaired by genetic disruption of CD3γ but not CD3δ, suggesting that CD3$\varepsilon\delta$ heterodimers are dispensable for both assembly and surface expression of these receptors but are required for signaling in mature $\alpha\beta$ T cells. Pre-TCRs are expressed early in thymic development on the surface of precursors of $\alpha\beta$ T cells, whereas $\gamma\delta$ T cells represent a separate lineage (27). Moreover, the CD3$\varepsilon\delta$ heterodimers are explicitly excluded during $\gamma\delta$ TCR assembly (19). Unlike CD3γ mutant mice, in which thymic development is blocked at the early $CD4^-CD8^-$ double negative (DN) stage, mice lacking CD3δ display $\alpha\beta$ T cell developmental arrest at the $CD4^+CD8^+$ double positive (DP) thymocyte stage (24, 26, 28). Such thymocytes are unable to undergo positive selection, which normally results from $\alpha\beta$ TCR interaction with self-pMHC molecules, to facilitate further differentiation into either mature $CD4^+$ or $CD8^+$ thymocytes, the immediate precursors of helper and cytotoxic T cells, respectively (29).

Structural elucidation of the TCR components is a prerequisite to understanding the initial events in the TCR signaling process. This is a daunting task, given the complexity of the TCR components and pMHC ligands as well as the ability of subtle variation in MHC-bound peptides to be detected by the TCR. To further investigate the basis of CD3 function in the TCR, we have focused on the structural determination of the CD3$\varepsilon\delta$ heterodimer, the final missing piece among the extracellular domains. To this end, we have designed a single-chain (sc) CD3$\varepsilon\delta$ heterodimer ectodomain using *Escherichia coli* expression and optimized *in vitro* refolding conditions. Here, we present the solution NMR structure of this scCD3$\varepsilon\delta$ heterodimer. Together with previously obtained structural and biochemical data, our recent results support a plausible model for the arrangement of the various TCR components and for early T

Abbreviations: TCR, T cell receptor; TM, transmembrane; pMHC, peptide bound to an MHC molecule; ITAM, immunoreceptor tyrosine-based activation motif; sc, single chain; rmsd, root-mean-square deviation; α-CP, TCR α-chain-connecting peptide.

Data deposition: The atomic coordinates and structure factors have been deposited in the Protein Data Bank, www.pdb.org (PDB ID code 1XMW).

[†]Z.-Y.J.S. and S.T.K. contributed equally to this work.

[§]Present address: Korea Research Institute of Bioscience and Biotechnology (KRIBB), Oun-Dong 52, Yusong-gu, Taejon 305-333, Korea.

[¶]To whom correspondence may be addressed. E-mail: ellis_reinherz@dfci.harvard.edu or gerhard_wagner@hms.harvard.edu.

[‖]The C2-set Ig fold typically contains ABE and GFCC′ strands in two β-sheets, whereas the C1-set Ig fold typically contains ABED and GFC strands.

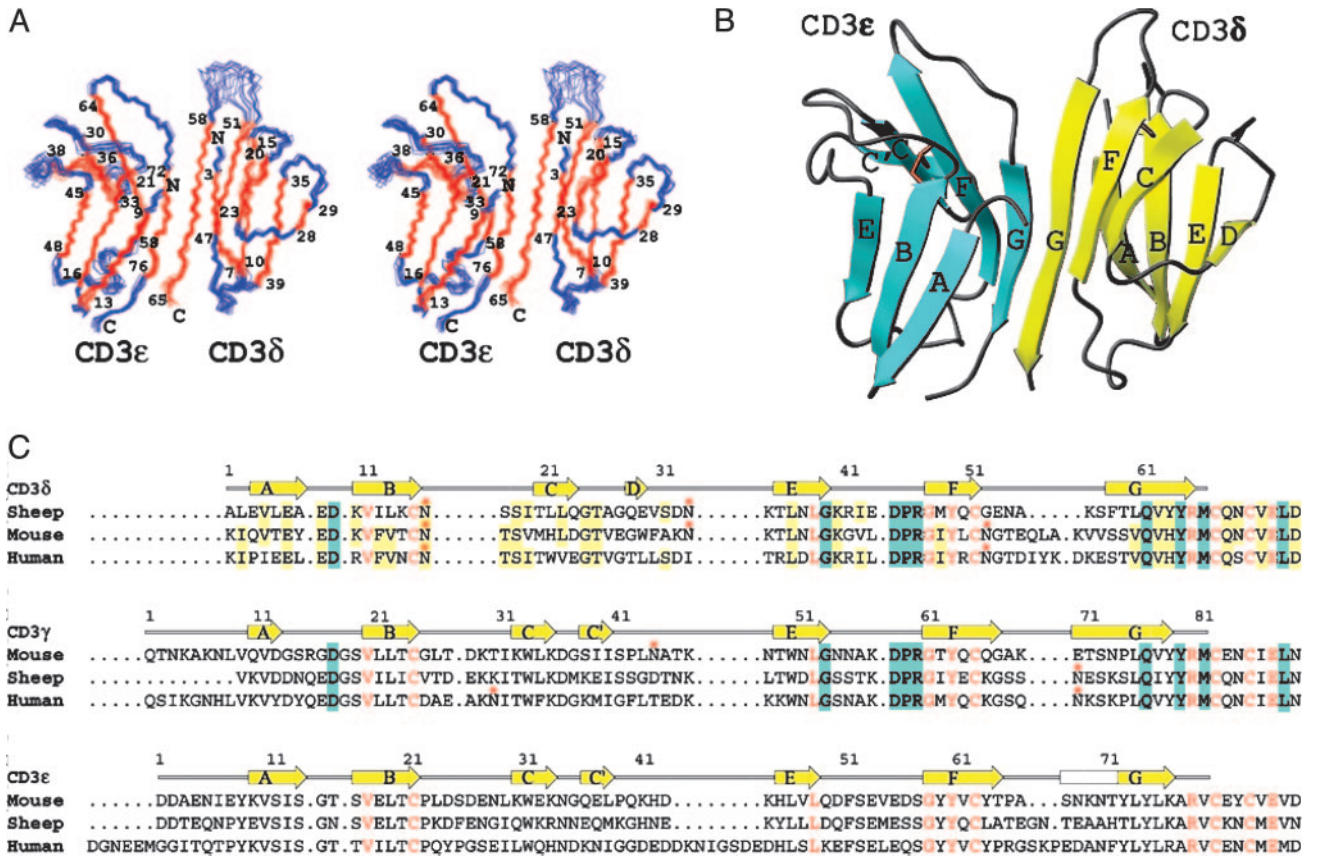

Fig. 1. NMR structures of CD3$\varepsilon\delta$ ectodomains. (*A*) Stereoview of an ensemble of the 15 final NMR structures of scCD3$\varepsilon\delta$, with the numbers indicating the beginning and end of the β-strands. The structure models shown span from Tyr-8ε to Val-79ε and from Leu-2δ to Arg-65δ, excluding the 33-aa linker. (*B*) Ribbon diagram of scCD3$\varepsilon\delta$ with β-strands of mouse CD3ε shown in cyan and of sheep CD3δ shown in yellow. The disulfide bond forming cysteine residues linking the β-sheets is shown in red, and the asparagine residues for glycan attachment are shown in blue. (*C*) Amino acid sequence alignments of CD3δ, CD3γ, and CD3ε from sheep, mouse, and human. The conserved residues among all sequences are shown in red letters. The residues conserved between CD3δ and CD3γ are highlighted in cyan. The residues that are conserved or highly homologous (including additional sequences from rat, monkey, and pig) in CD3δ are highlighted in yellow. The β-strands shown above the sequences are taken from sheep CD3δ and mouse CD3ε and CD3γ. Glycosylation sites are indicated with asterisks.

cell signaling mechanisms linked to thymic selection events and T cell activation.

Methods

Cloning, Expression, Refolding, and Purification of CD3$\varepsilon\delta$. Covalently linked scCD3$\varepsilon\delta$ constructs were expressed, refolded, and purified (unpublished results). Briefly, this constructed gene, which encodes a murine CD3ε fragment (residue ID 22–100 of Swiss-Prot P22646), a 33-aa flexible linker, and a sheep CD3δ fragment (residue ID 23–88 of Swiss-Prot P18438), was cloned into a pET11a expression vector, and recombinant scCD3$\varepsilon\delta$ proteins were produced as inclusion bodies in *E. coli* B834(DE3). To find an optimized refolding condition, refolding efficiency in the 16 different conditions of the FoldIt kit (Hampton Research, Aliso Viejo, CA) was primarily monitored by surface plasmon resonance using the conformation-specific anti-murine CD3ε mAb 17A2 (BD Biosciences Pharmingen) (30) and confirmed by gel filtration chromatography. The optimal refolding buffer contained 55 mM Mes (pH 6.5), 264 mM NaCl, 11 mM KCl, 2.2 mM $MgCl_2$, 2.2 mM $CaCl_2$, 440 mM sucrose, 0.1 mM reduced glutathione, 1 mM oxidized glutathione, and 0.5× complete protease inhibitor mixture (Roche Applied Science). After *in vitro* refolding, soluble and monomeric CD3 proteins were purified by gel filtration on a Superdex 75 column (Amersham Biosciences).

NMR Spectroscopic Studies of scCD3$\varepsilon\delta$. The solution structure of scCD3$\varepsilon\delta$ was determined by NMR spectroscopy using isotopically labeled proteins expressed from *E. coli*. Standard multidimensional NMR experiments (31) were carried out primarily on a Bruker (Billerica, MA) Avance 500 spectrometer equipped with a cryogenic probe using 0.3 ml of 0.5 mM isotopically labeled scCD3$\varepsilon\delta$ samples in buffer (50 mM NaCl/17 mM $NaPO_4$, pH 7.4) at 25°C. IBIS software (32) was used in obtaining the backbone NMR assignments. Backbone dihedral angle restraints were obtained by using TALOS software (33) based on assigned ^{13}C chemical shifts. Distance nuclear Overhauser effect (NOE) restraints were obtained from ^{15}N- and ^{13}C-separated 3D NOESY as well as conventional 2D NOESY data sets. Hydrogen bond restraints were derived from NOE distance restraints after the initial protein fold was determined to improve convergence of calculated structures. The final NMR structures (Fig. 1*A*), with statistical results shown in Table 1, were calculated by using X-PLOR software (34). The coordinates have been deposited in the Protein Data Bank (PDB ID code 1XMW).

Modeling TCR/CD3 Extracellular Domain Organizations. We searched for plausible docking models for the $\alpha\beta$ TCR and CD3 extracellular domains using TREEDOCK software (35) while incorporating known experimental results. The coordinates were taken from an N15 TCR (PDB ID code 1NFD) and the most representative NMR structures of scCD3$\varepsilon\gamma$ (PDB ID code 1JBJ) and scCD3$\varepsilon\delta$ (PDB ID

Table 1. Statistics for final 15 NMR structures

NOE distance restraints	1,610
Intraresidue	370
Medium range (≤4)	560
Long range (>4)	680
Hydrogen bond restraints	116
Backbone dihedral angle restraints	193
Ramanchandran plot, %	
Most favored region	73.5
Additionally allowed region	22.9
Generously allowed region	3.0
Disallowed region	0.5
Backbone ⟨rmsd⟩ from mean structure, Å	0.62

The final 15 NMR structures were selected from 25 models (rmsd = 0.67 Å) calculated by using XPLOR. The criteria for selection were based on lowest nuclear Overhauser effect (NOE) energy function, minimal number of Φ, Ψ angles in disallowed regions of the Ramachandran plots, no NOE violations of >0.35 Å, and no angular violations of >5°. The statistical results exclude N-terminal residues 1–7 from CD3ε, the N- and C-terminal residue of CD3δ, and 33 residues in the linker region.

code 1XMW). Specifically, for CD3$\varepsilon\gamma$ docking, four residues from the TCR Cα AB loop within a pocket formed between the TCR Cα CD and EF loops and the TCR Cβ FG loop were used as docking targets, and the models were further selected to best accommodate an H57 Fab fragmont bound to the TCR Cβ FG loop. CD3$\varepsilon\delta$ was docked to the TCR α-chain by using residues from the constant domain as docking targets, and the models were further selected by avoiding clashes between modeled glycans on TCR and CD3δ. The linker residues from CD3 were excluded from these models before docking. A representative model of the associated TCR/CD3 extracellular domains was selected visually for preparing the figures.

Results

Production of Heterodimeric CD3$\varepsilon\delta$ Extracellular Domain Fragments. We designed N-terminal CD3$\varepsilon\delta$ ectodomain fragments that were truncated at Val-79ε of mouse CD3ε and Met-66δ of sheep CD3δ sequences. These segments were covalently linked between the C terminus of CD3ε and the N terminus of CD3δ with a 33-aa peptide linker identical to that used in the scCD3$\varepsilon\gamma$ construct (30). The sheep CD3δ chain was chosen instead of a murine orthologue to reduce surface-exposed hydrophobic residues and increase solubility. The residues at the dimer interface of CD3$\varepsilon\delta$ are highly conserved between murine and sheep species, as discussed below (Figs. 1*C* and 5, which is published as supporting information on the PNAS web site). $^{15}N^{1}H$ 2D NMR spectra indicated that only the purified chimera scCD3$\varepsilon\delta$ (murine CD3ε and sheep CD3δ) with the 33-aa peptide linker was structured and stable under physiological conditions (unpublished results), compared with the multiple murine scCD3$\varepsilon\delta$ constructs tested. The NMR results suggest that the 33-aa linker is highly mobile and does not interact with the CD3 domains (possibly looping around the CD3ε domain across the GFC face in a highly flexible manner).

Domain Characterization of CD3$\varepsilon\delta$. As shown in Fig. 1*A* and *B*, both sheep CD3δ and murine CD3ε are Ig domains consisting of two β-sheets each. The murine CD3ε domains in the CD3$\varepsilon\delta$ and CD3$\varepsilon\gamma$ solution structures are extremely similar (Fig. 2 *A* and *B*) (17), although the NMR structures were obtained at different pH conditions (pH 4.5 for CD3$\varepsilon\gamma$ and pH 7.4 for CD3$\varepsilon\delta$). The average backbone root-mean-square deviation (rmsd) between the two CD3ε domains is 1.45 Å when superimposed for all but the six N-terminal residues, whereas the average backbone rmsd when superimposed for 31 residue pairs from six β-strands (A, B, E, G, F, and C strands) is only 0.92 Å. The small

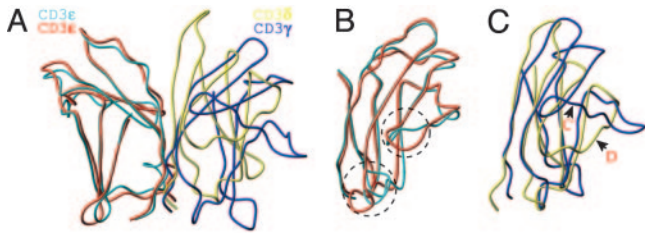

Fig. 2. Comparison of CD3 structures. (*A*) Schematic diagram showing the superimposition of scCD3$\varepsilon\delta$ with scCD3$\varepsilon\gamma$ using selected backbone atoms from the CD3ε subunits as described in the text. The mouse CD3ε and sheep CD3δ from scCD3$\varepsilon\delta$ are shown in cyan and yellow, respectively. The mouse CD3ε and CD3γ from scCD3$\varepsilon\gamma$ are shown in red and blue, respectively. (*B*) Superimposed CD3ε domains rotated 180° relative to *A*. Regions showing structural differences are highlighted by dashed circles. (*C*) Superimposition of sheep CD3δ with mouse CD3γ (17) as described in the text.

deviations in the CC′ loop and EF loop (Fig. 2*B*) are due to the fact that these loops do not converge well in the CD3$\varepsilon\gamma$ structure but are better defined in the CD3$\varepsilon\delta$ structure.

The CD3δ domain, on the other hand, has a different fold than murine CD3ε and CD3γ, which adopt C2-set Ig folds. The front face of CD3δ contains G, F, and C β-strands, but not the C′ strand present in both CD3ε and CD3γ. This C′ strand, predicted by sequence alignment (17), is translocated to join the back face, becoming a D strand. Hence, the back face of CD3δ contains A, B, E, and D β-strands, characteristic of an Ab constant domain-like C1-set fold. The BC loop connecting the two disulfide-linked β-sheets of CD3δ is extremely short, which is, in part, responsible for the comparatively small Ig domain size (66 residues) (Fig. 1 *B* and *C*).

Domain Association of the CD3$\varepsilon\delta$ Heterodimer. The extracellular domains of CD3ε and CD3δ in scCD3$\varepsilon\delta$ associate with each other via their respective G strands, which form a parallel β-strand pair with extensive hydrogen bonds (Figs. 1*B* and 6, which is published as supporting information on the PNAS web site), in a manner similar to that in scCD3$\varepsilon\gamma$ (17). However, when both heterodimer structures are aligned according to the backbone atoms of five β-strands (A, B, E, F, and G strands) of the CD3ε domains, the CD3δ and CD3γ domains appear to have very different overall shapes and orientations (Fig. 2*A*). The CD3δ ectodomain is more upright, because the two β-sheets are more parallel to each other than those in CD3γ. This appearance is due to several factors. First, the F strand in CD3δ is more parallel to the G strand than to the C strand (which contains a β-bulge) within the CD3δ domain. Second, there are more hydrogen bonds formed between the two G strands at the CD3$\varepsilon\delta$ interface than those in murine CD3$\varepsilon\gamma$. Third, the BC loop is very short (see above) and cuts across the two β-sheets, preventing the FG loop from bending to the ABED face as in CD3ε and CD3γ. Finally, additional hydrogen bonds, involving Pro-45δ and Arg-46δ residues just before the F strand, with Tyr-64δ in the G strand and Thr-25δ in the CD loop, respectively, also help to straighten the GFC β-sheet (Fig. 6).

Fig. 2*A* shows that CD3δ is closer to the pseudo 2-fold axis of the CD3$\varepsilon\delta$ heterodimer, whereas the GFCC′ face of CD3γ is rotated away from CD3ε in CD3$\varepsilon\gamma$. It appears that there is a more pronounced cleft between the two CD3 ectodomains in CD3$\varepsilon\gamma$ than in CD3$\varepsilon\delta$, which is possibly important for association with the TCR $\alpha\beta$ dimer. However, the core region of the sheep CD3δ domain superimposes very well with mouse CD3γ as shown in Fig. 2*C*. The average backbone rmsd when superimposing 21 residue pairs from the homologous regions of five β-strands (A, B, E, G, and F strands) is only 1.18 Å between CD3δ and mouse CD3γ.

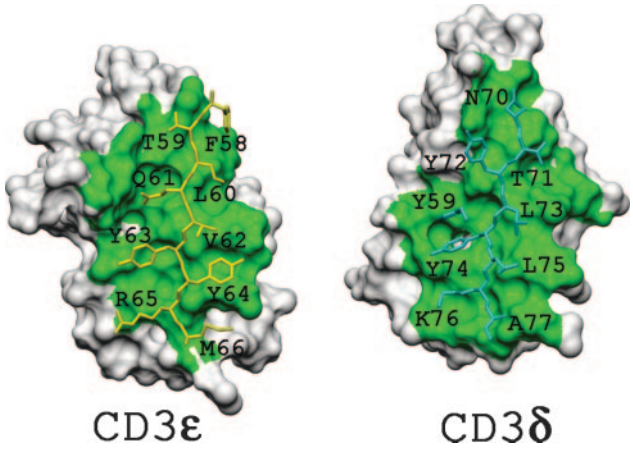

Fig. 3. Interface surfaces of CD3ε and CD3δ. The key residues from CD3ε (cyan) and CD3δ (yellow) binding partners are shown as stick models on the labeled subunit surfaces. The two faces are in an open-book orientation from the same scCD3$\varepsilon\delta$ complex, with contact surfaces shown in green.

The Interface of the CD3$\varepsilon\delta$ Heterodimer. The dimer interface of scCD3$\varepsilon\delta$ (Fig. 3) is very similar to that of CD3$\varepsilon\gamma$ (17). The total buried area is 1,546 Å^2, larger than the 1,306 Å^2 of the murine CD3$\varepsilon\gamma$ interface, as determined for representative NMR structures by using NACCESS software (http://wolf.bms.umist.ac.uk/naccess). This increase is mostly the result of additional contacts near the top of the G strands (Phe-58δ, Thr-59δ, and Asn-70ε) between the two CD3 domains, consistent with the more upright CD3δ structure. The residues in CD3δ that contribute >10 Å^2 each to the buried surface area at the dimer interface include Ser-57δ, Phe-58δ, Thr-59δ, Leu-60δ, Gln-61δ, Tyr-63δ, Tyr-64δ, Arg-65δ, and Met-66δ from the G strand, Val-4δ and Glu-6δ from the A strand, Met-48δ from the F strand, and Arg-41δ from the EF loop. All of these residues (except for Arg-41δ, Ser-57δ, and Phe-58δ) are highly conserved or homologous between sheep and murine CD3δ (Fig. 1*C*), justifying our approach of creating a chimeric mouse/sheep CD3$\varepsilon\delta$ heterodimer for solution structural studies under physiological conditions.

The residues in murine CD3ε and sheep CD3δ domains that are important for dimer association (mostly from the G strands) are shown in Fig. 3 as stick models on the background of the molecular surface of their binding partners. The key residues from CD3ε (shown in cyan) are three tyrosine residues, Tyr-59ε, Tyr-72ε, and Tyr-74ε, that protrude into cavities on the CD3δ surface. The hydrophobic residues on the opposite side of the G strand plus residues from the A strand in CD3ε form the base of cavities to accommodate residues at the interface of CD3δ. In addition, Tyr-64δ and Lys-76ε form an aromatic ring–aliphatic chain hydrophobic contact, whereas Gln-61δ and Tyr-8ε (data not shown) form a side chain-to-backbone hydrogen bond.

Comparison of Regions Between C and E Strands of CD3δ and CD3γ. The C strand in CD3δ is shifted unexpectedly by two residues with respect to the amino acid sequence-based alignment with CD3γ (17) (Fig. 1*C*), causing the BC loop, which contains only four residues, to form a tight turn that cuts across the β-sheets (Fig. 1 *A* and *B*). A highly conserved tryptophan residue in the central position of the C strand of CD3ε and CD3γ is missing from the sheep and mouse CD3δ sequence and is replaced by a hydrophobic isoleucine residue (or valine in mouse CD3δ) just before the C strand in sheep CD3δ. A β-bulge near the end of the C-strand in CD3δ disrupts hydrogen bonds necessary for C′ strand formation (Fig. 1*B*), causes the side chain of residue Leu-21δ to tilt toward the center of the CD loop region, and stabilizes it by interacting with Leu-36δ from the E strand (Fig. 7, which is published as supporting information on the PNAS web site). The residue Leu-22δ in the same β-bulge is also tilted toward residue Met-48δ on the F strand to allow more hydrophobic contacts. In addition, the region of the D strand and DE loop of CD3δ, but not CD3γ, is negatively charged (Fig. 8, which is published as supporting information on the PNAS web site).

The DE loop of sheep CD3δ is bent outward, so that the putative glycan anchored to residue Asn-33δ is pointing up and away from another putative glycan anchored to residue Asn-16δ in the beginning of the BC loop (Fig. 1*B*). This unusual orientation may be caused by an apparent hydrogen bond between the backbone atoms of a conserved Ser-18δ residue in the BC loop and the Asn-33δ residue in the DE loop (Fig. 7). Perhaps this is a substitution for the canonical hydrogen bond formed between the side-chain NH group of the tryptophan residue missing from the CD3δ C strand and the backbone carbonyl of a residue in the C′E loop, serving to strengthen the stability of the Ig domain. Mouse and human CD3δ both have an additional glycosylation site at the beginning of the FG loop so that the top of each CD3δ ectodomain would be covered heavily with two to three complex-sugar systems.

Discussion

In the present study, we have structurally characterized a CD3$\varepsilon\delta$ heterodimer by NMR spectroscopy. The CD3ε domains in both CD3$\varepsilon\gamma$ and CD3$\varepsilon\delta$ structures are nearly identical (Fig. 2 *A* and *B*), consistent with the conservation of residues in CD3γ and CD3δ that interact with CD3ε. Not surprisingly, mAbs with specificity for CD3ε in mouse or human (i.e., hamster anti-mouse CD3ε 145-2C11, rat anti-mouse CD3ε 17A2, or mouse anti-human CD3ε OKT3) immunoprecipitate both CD3$\varepsilon\gamma$ and CD3$\varepsilon\delta$ heterodimers from T cells (6, 18). The overall average backbone rmsd of scCD3$\varepsilon\delta$ is 0.62 Å (Table 1), compared with 0.95 Å for murine scCD3$\varepsilon\gamma$ (17). The high-quality NMR data of scCD3$\varepsilon\delta$ herein offer excellent characterization of all of the loop regions except for one segment of the FG loop in CD3δ.

The murine and sheep CD3δ sequences are highly homologous (amino acid identity of 47%), especially in the G strand at the CD3$\varepsilon\delta$ dimer interface. However, there is virtually no consensus sequence in the segment between the C and E strands of CD3δ from different species, and a highly conserved buried tryptophan residue in the respective C strands is missing in sheep, mouse, and rat. The conformation of this region, with the translocated D strand in particular, may be determined by three highly conserved features, namely an N(S/T)S glycosylation site in the short BC loop, a GT tight turn in the CD loop, and an additional NKT glycosylation site conserved among sheep, mouse, and rat near the N terminus of the E strand. The upright orientation of CD3δ and the unique conformations of the BC and DE loops are likely to guide the attached glycans away from the membrane (Fig. 1*B*), which, we reason, is structurally important for the association between CD3$\varepsilon\delta$ and TCR $\alpha\beta$ dimers.

Our first attempt to investigate possible interactions between the CD3$\varepsilon\delta$ ectodomain fragment and TCR molecule, using ^{15}N-labeled scCD3$\varepsilon\delta$ titrated with unlabeled deglycosylated N15 TCR $\alpha\beta$ dimer (truncated at the interchain disulfide bond-forming cysteine residues near the C termini) failed to show any detectable binding (see supporting information). In search of a putative contact face between the CD3δ and TCR $\alpha\beta$-chains, we examined conserved residues in CD3δ from different species. The conserved residues in CD3δ are concentrated at the bottom half of the domain, in the hydrophobic core of the protein, or in the unique small BC loop (Figs. 1*C* and 5). Additional homologous residues are found at the dimer interface and the B and C strands. Most of these residues appear to be important for the structural integrity of the CD3δ domain or the CD3$\varepsilon\delta$ dimeric interface. Most significant conserved regions unique to CD3δ (not found in CD3ε and CD3γ) include the AB loop with an ED(K/R) pattern, and the N-terminal half of the

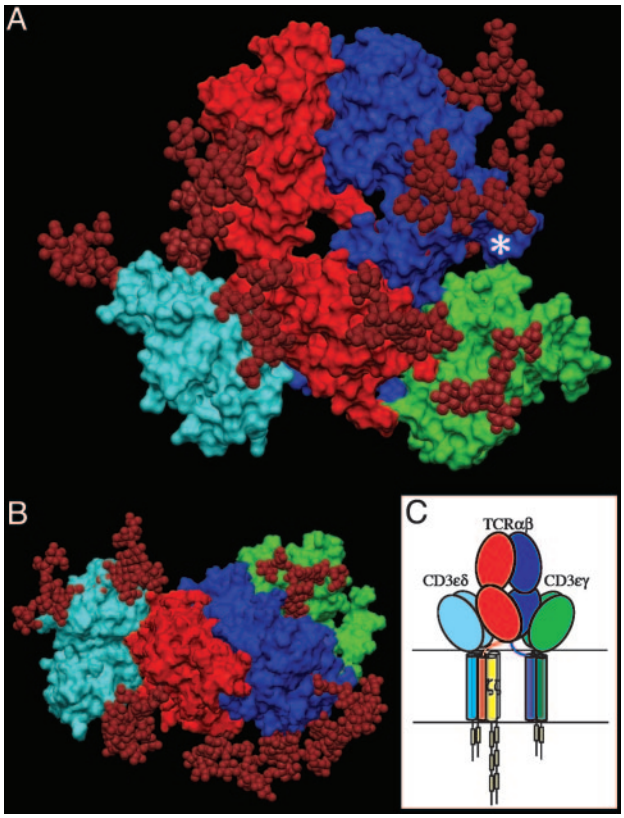

Fig. 4. A docking model depicting potential ectodomain interactions of CD3 and $\alpha\beta$ TCR. (*A*) Front view with the cell membrane at the bottom. The TCR α-chain is shown in red, the TCR β-chain is shown in blue, CD3$\varepsilon\gamma$ is shown in green, CD3$\varepsilon\delta$ is shown in cyan, and glycans are shown in maroon. Glycans (three in TCRα, four in TCRβ, two in sheep CD3δ, and one in mouse CD3γ adducts) are represented by models taken from Wyss *et al.* (52). An asterisk marks the Cβ FG loop where the H57 Fab fragment binds. (*B*) Top view of the antigen-binding site. The structure is rotated 90° about the *x* axis relative to *A*. (*C*) Association topology of TCR and CD3 chains, based on experimental evidence referred to in the text and with the same orientation as in *A*. The yellow rectangles represent individual ITAMs in the CD3 cytoplasmic tails.

EF loop with a K(R/G)(I/V)(L) pattern near the bottom of the CD3δ domain (Figs. 1*C* and 5). We hypothesize that the appearance of these conserved regions may participate in an interaction with the highly conserved membrane-proximal TCR α-chain-connecting peptide (α-CP), the peptide linking the C terminus of the TCRα constant domain with the N terminus of the TM helix. In this regard, removal of the FETDxNLN sequence within α-CP blocks positive selection in the thymus, similar to the consequence of CD3δ gene deletion (26, 36). Our preliminary NMR binding experiments failed to confirm such an interaction using a synthetic α-CP (see *Supporting Text*, which is published as supporting information on the PNAS web site). However, this result is inconclusive because the synthetic α-CP may lack structure in the absence of a membrane context or other essential TCR components.

Having structures of TCR $\alpha\beta$, CD3$\varepsilon\gamma$, and CD3$\varepsilon\delta$ heterodimers permits us to construct a plausible model for the topology of assembled subunit ectodomains of the TCR (Fig. 4 *A* and *B*). Given that CD3ζ has an ectosegment only 9-aa long, its extracellular segment is omitted from the figure, as are the connecting peptides of TCR α- and β-chains and the RxCxxCxE stalk regions proximal to the TM segments of CD3ε, CD3γ, and CD3δ. However, this rendering incorporates the consequences of several known TCR characteristics: TM charge pairs involving TCR subunit chain associations, CD3ε–CD3δ–TCRα–CD3ζ–CD3ζ as one cluster and CD3ε–CD3γ–TCRβ as a second cluster (37, 38), extracellular domain associations involving other *in vitro* chain-association data (7, 39), TCR crosslinking results (6, 40), and proximity of one CD3ε subunit to the TCR Cβ FG loop by quantitative T cell surface immunofluorescent Ab binding analysis (9). In addition, structural insights from crystallographic data on the glycosylated N15 TCR in complex with the H57 Fab fragment and the likely position of glycans in both CD3$\varepsilon\gamma$ and CD3$\varepsilon\delta$ uncovered herein are considered. Specifically, CD3$\varepsilon\gamma$ is presumed to be near the pocket formed between the TCR Cα CD and EF loops and the Cβ FG loop (9, 41). Residues in the TCR Cα AB loop, which shows significant conformational change for an LC13 TCR upon pMHC binding (42), were used as target sites for CD3$\varepsilon\gamma$ docking in the initial search for possible docking models. CD3$\varepsilon\delta$ is docked on the opposite site of the TCR $\alpha\beta$ domain where there is less glycan to interfere with the more heavily glycosylated CD3δ subunit (Fig. 4*B*), consistent with known TCRα and CD3δ TM associations.

Immediately evident is the central position of the TCR $\alpha\beta$ heterodimer with a vertical dimension of 80 Å projecting from the cell membrane, flanked on either side by the shorter (40 Å) CD3 heterodimers, CD3$\varepsilon\delta$ on the "left" TCRα side and CD3$\varepsilon\gamma$ on the "right" TCRβ side. Note that the widths of the CD3$\varepsilon\delta$ and CD3$\varepsilon\gamma$ components, 50 Å and 55 Å, respectively, are comparable with that of the TCR$\alpha\beta$ heterodimer (58 Å) and together (excluding glycans) span ≈160 Å. These flanking CD3 components will likely impede lateral movement of the TCR $\alpha\beta$ heterodimer upon pMHC binding. As previously noted for CD3$\varepsilon\gamma$ (17), the intradomain disulfide bridge between cysteine residues on the B and F strands at the center of each CD3$\varepsilon\delta$ domain reinforces the domain structure. Further rigidity for potential signal transduction comes from the paired G β-strands in each CD3 heterodimer, coupled with the conserved RxCxxCxE cysteine-coordinated stalks.

The length of the CD3 subunit stalks is typical for TM proteins (5–10 aa) observed, for example, for CD2, CD4 and CD58. On the other hand, the connecting peptides found in TCRα (25–26 residues) and TCRβ (19 residues) are long. The latter are probably mandated by a requirement for a linker segment of sufficient length to span the 50 Å from the end of the interchain disulfide of the TCRα constant domain to the associated CD3ε and CD3δ TM segments that are juxtaposed for charge pairing (i.e., the TCRα lysine and aspartate residues of CD3ε and CD3δ TM, respectively). Similar considerations must be applied to the TCRβ-connecting peptide, including charge pairing of the TM TCRβ lysine with an aspartic and a glutamic acid residue of CD3ε and CD3γ TM, respectively. Note that the TCRα TM also includes an arginine residue that is thought to form a charged pair with an aspartate residue in each of the CD3ζ TM segments (37).

Given crystallographic details on TCR, CD4, and CD8 interactions with pMHC I and pMHC II ligands (43), it is clear that the CD4 and CD8 coreceptors are located at left in Fig. 4 *A* and *B*, adjacent to CD3$\varepsilon\delta$ when binding to the same pMHC ligand as the TCR. Not surprisingly, CD3δ couples the TCR with lipid raft-associated CD8$\alpha\beta$ required for effective activation and positive selection of $CD8^+$ T cells (44). Although the relatively flexible CD8 stalk region poses no steric constraints for concurrent TCR ligation, CD4 is a rigid concatamer with four Ig domains comprising its extracellular segment (45, 46). Nevertheless, structural analysis (43) shows that the membrane-proximal ends of CD4 and TCR$\alpha\beta$ are 100 Å apart, providing ample space for the CD3$\varepsilon\delta$ heterodimer to occupy a position between the two T cell surface molecules.

The multiple N-linked glycan adducts are prominent components of the TCR complex (Fig. 4 *A* and *B*). In addition to guiding pMHC ligands to the TCR recognition surface, these glycans may play a regulatory role by contributing to a galectin–glycoprotein lattice (47). In this regard, a deficiency in the β1,6-*N*-acetylglucosaminyltransferase V (Mgat5) enzyme crucial in the N-glycosylation pathway lowers the T cell activation threshold by enhancing TCR

clustering. The more heavily glycosylated CD3δ subunit may influence TCR subunit assembly through steric constraints. However, the distinct conformation of Cδ relative to Cα and/or differences in their respective connecting peptides are likely responsible for exclusion of CD3εδ from association with TCR γδ heterodimers (36, 48). The distribution of glycans in the model shown in Fig. 4*A* is also consistent with the lack of mAbs raised against the native CD3δ and CD3γ subunits.

We hypothesize that, based on the structures of CD3εδ and CD3εγ, highly selective TCR signaling may require dynamic interaction rather than static on-and-off switching, such that the interfaces between the extracellular domains of the TCR αβ heterodimer and CD3 dimers may be quite small. With this current model, no detailed information on the interfaces is warranted, being one of a range of acceptable structures. Nonetheless, we envisage the ectodomains of TCR αβ-chains being supported by the CD3 heterodimers, whereas components of the TCR αβ dimer, such as the Cβ FG loop (41) and the α-CP (36, 49), may serve as levers to control vertical movements of CD3 subunits for signal transduction through the critical TM segments. Given the apparently weak ectodomain association between CD3 and TCR αβ heterodimers (this paper and ref. 41 and references therein), it is possible that this assembly undergoes dynamic quaternary change upon TCR ligation, thereby affecting cytoplasmic CD3 signaling regions.

According to the model in Fig. 4*C*, there are two separate clusters of TM segments: the five helices of the CD3ε–CD3δ–TCRα–CD3ζ–CD3ζ component lie closer to the TCRα subunit, and the three helices of the CD3ε—CD3γ–TCRβ component lie closer to the TCRβ subunit (37). The cluster shown at left in Fig. 4*C* has eight cytoplasmic ITAMs, one in CD3ε, one in CD3δ, and three in each CD3ζ, whereas the cluster shown at right in Fig. 4*C* has two ITAMs, one in CD3ε and one in CD3γ. Given that the copy number of ITAMs augments TCR signaling strength (50), it is easy to imagine how signaling will be dramatically attenuated when this cluster is perturbed by CD3δ deletion or α-CP mutation. Because positive selection involves the weakest of self–pMHC–ligand interactions, amplification of signal through multiple ITAMs in both clusters is critical for TCR-mediated signaling (51). Pre-TCR signaling must largely rely on the right cluster (Fig 4*C*) because pTα, the α-chain surrogate, lacks a V domain for signaling (27). As additional details begin to emerge about these ectodomains and membrane-proximal and TM segments, the structural basis of TCR signaling through its amazing set of components will become clear.

We thank Drs. Jia-huai Wang, Kristine Brazin, Robert Mallis, and Linda Clayton for thoughtful discussion and careful review of the manuscript. This work was supported by National Institutes of Health Grants AI19807 (to E.L.R.) and AI37581 and GM47467 (to G.W.). S.T.K. was partially supported by a postdoctoral fellowship from the Korea Science and Engineering Foundation (KOSEF).

1. Reinherz, E. L., Meuer, S. C. & Schlossman, S. F. (1983) *Immunol. Rev.* **74,** 83–112.
2. Hayes, S. M., Shores, E. W. & Love, P. E. (2003) *Immunol. Rev.* **191,** 28–37.
3. Davis, M. M. & Bjorkman, P. J. (1988) *Nature* **334,** 395–402.
4. Alarcon, B., Berkhout, B., Breitmeyer, J. & Terhorst, C. (1988) *J. Biol. Chem.* **263,** 2953–2961.
5. de la Hera, A., Muller, U., Olsson, C., Isaaz, S. & Tunnacliffe, A. (1991) *J. Exp. Med.* **173,** 7–17.
6. Koning, F., Maloy, W. L. & Coligan, J. E. (1990) *Eur. J. Immunol.* **20,** 299–305.
7. Manolios, N., Letourneur, F., Bonifacino, J. S. & Klausner, R. D. (1991) *EMBO J.* **10,** 1643–1651.
8. Punt, J. A., Roberts, J. L., Kearse, K. P. & Singer, A. (1994) *J. Exp. Med.* **180,** 587–593.
9. Ghendler, Y., Smolyar, A., Chang, H. C. & Reinherz, E. L. (1998) *J. Exp. Med.* **187,** 1529–1536.
10. Irving, B. A. & Weiss, A. (1991) *Cell* **64,** 891–901.
11. Letourneur, F. & Klausner, R. D. (1992) *Science* **255,** 79–82.
12. Reth, M. (1989) *Nature* **338,** 383–384.
13. Exley, M., Varticovski, L., Peter, M., Sancho, J. & Terhorst, C. (1994) *J. Biol. Chem.* **269,** 15140–15146.
14. Isakov, N., Wange, R. L., Burgess, W. H., Watts, J. D., Aebersold, R. & Samelson, L. E. (1995) *J. Exp. Med.* **181,** 375–380.
15. Ravichandran, K. S., Lee, K. K., Songyang, Z., Cantley, L. C., Burn, P. & Burakoff, S. J. (1993) *Science* **262,** 902–905.
16. Sunder-Plassmann, R., Lialios, F., Madsen, M., Koyasu, S. & Reinherz, E. L. (1997) *Eur. J. Immunol.* **27,** 2001–2009.
17. Sun, Z. J., Kim, K. S., Wagner, G. & Reinherz, E. L. (2001) *Cell* **105,** 913–923.
18. Kjer-Nielsen, L., Dunstone, M. A., Kostenko, L., Ely, L. K., Beddoe, T., Mifsud, N. A., Purcell, A. W., Brooks, A. G., McCluskey, J. & Rossjohn, J. (2004) *Proc. Natl. Acad. Sci. USA* **101,** 7675–7680.
19. Hayes, S. M. & Love, P. E. (2002) *Immunity* **16,** 827–838.
20. Malissen, M., Gillet, A., Ardouin, L., Bouvier, G., Trucy, J., Ferrier, P., Vivier, E. & Malissen, B. (1995) *EMBO J.* **14,** 4641–4653.
21. Malissen, M., Gillet, A., Rocha, B., Trucy, J., Vivier, E., Boyer, C., Kontgen, F., Brun, N., Mazza, G. & Spanopoulou, E. (1993) *EMBO J.* **12,** 4347–4355.
22. Love, P. E., Shores, E. W., Johnson, M. D., Tremblay, M. L., Lee, E. J., Grinberg, A., Huang, S. P., Singer, A. & Westphal, H. (1993) *Science* **261,** 918–921.
23. Liu, C. P., Ueda, R., She, J., Sancho, J., Wang, B., Weddell, G., Loring, J., Kurahara, C., Dudley, E. C. & Hayday, A. (1993) *EMBO J.* **12,** 4863–4875.
24. Haks, M. C., Krimpenfort, P., Borst, J. & Kruisbeek, A. M. (1998) *EMBO J.* **17,** 1871–1882.
25. DeJarnette, J. B., Sommers, C. L., Huang, K., Woodside, K. J., Emmons, R., Katz, K., Shores, E. W. & Love, P. E. (1998) *Proc. Natl. Acad. Sci. USA* **95,** 14909–14914.
26. Dave, V. P., Cao, Z., Browne, C., Alarcon, B., Fernandez-Miguel, G., Lafaille, J., de la Hera, A., Tonegawa, S. & Kappes, D. J. (1997) *EMBO J.* **16,** 1360–1370.
27. von Boehmer, H. & Fehling, H. J. (1997) *Annu. Rev. Immunol.* **15,** 433–452.
28. Delgado, P., Fernandez, E., Dave, V., Kappes, D. & Alarcon, B. (2000) *Nature* **406,** 426–430.
29. Werlen, G., Hausmann, B., Naeher, D. & Palmer, E. (2003) *Science* **299,** 1859–1863.
30. Kim, K. S., Sun, Z. Y., Wagner, G. & Reinherz, E. L. (2000) *J. Mol. Biol.* **302,** 899–916.
31. Ferentz, A. E. & Wagner, G. (2000) *Q. Rev. Biophys.* **33,** 29–65.
32. Hyberts, S. G. & Wagner, G. (2003) *J. Biomol. NMR* **26,** 335–344.
33. Cornilescu, G., Delaglio, F. & Bax, A. (1999) *J. Biomol. NMR* **13,** 289–302.
34. Brünger, A., Adams, P., Clore, G., DeLano, W., Gros, P., Grosse-Kunstleve, R., Jiang, J.-S., Kuszewski, J., Nilges, N., Pannu, N., *et al*. (1998) *Acta Crystallogr. D* **54,** 905–921.
35. Fahmy, A. & Wagner, G. (2002) *J. Am. Chem. Soc.* **124,** 1241–1250.
36. Backström, B. T., Muller, U., Hausmann, B. & Palmer, E. (1998) *Science* **281,** 835–838.
37. Call, M. E., Pyrdol, J., Wiedmann, M. & Wucherpfennig, K. W. (2002) *Cell* **111,** 967–979.
38. Call, M. E., Pyrdol, J. & Wucherpfennig, K. W. (2004) *EMBO J.* **23,** 2348–2357.
39. Manolios, N., Kemp, O. & Li, Z. G. (1994) *Eur. J. Immunol.* **24,** 84–92.
40. Brenner, M. B. (1985) *Cell* **40,** 183–190.
41. Wang, J., Lim, K., Smolyar, A., Teng, M.-K., Liu, J.-H., Tse, A. G. T., Liu, J., Hussey, R. E., Chishti, Y., Thomson, C. T., *et al*. (1998) *EMBO J.* **17,** 10–26.
42. Kjer-Nielsen, L., Clements, C. S., Purcell, A. W., Brooks, A. G., Whisstock, J. C., Burrows, S. R., McCluskey, J. & Rossjohn, J. (2003) *Immunity* **18,** 53–64.
43. Wang, J.-H. & Reinherz, E. L. (2001) *Mol. Immunol.* **38,** 1039–1049.
44. Doucey, M. A., Goffin, L., Naeher, D., Michielin, O., Baumgartner, P., Guillaume, P., Palmer, E. & Luescher, I. F. (2003) *J. Biol. Chem.* **278,** 3257–3264.
45. Moody, A. M., Chui, D., Reche, P., Priatel, J. J., Marth, J. D. & Reinherz, E. L. (2001) *Cell* **107,** 501–512.
46. Wu, H., Kwong, P. D. & Hendrickson, W. A. (1997) *Nature* **387,** 527–530.
47. Demetriou, M., Granovsky, M., Quaggin, S. & Dennis, J. M. (2001) *Nature* **409,** 733–739.
48. Allison, T. J., Winter, C. C., Fournie, J.-J., Bonneville, M. & Garboczi, D. N. (2001) *Nature* **411,** 820–824.
49. Werlen, G., Hausmann, B. & Palmer, E. (2000) *Nature* **406,** 422–426.
50. Van Oers, N. S. C., Love, P. E., Shores, E. W. & Weiss, A. (1998) *J. Immunol.* **160,** 163–170.
51. Haks, M. C., Pepin, E., van den Brakel, J. H. N., Smeele, S. A. A., Belkowski, S. M., Kessels, H. W. H. G., Krimpenfort, P. & Kruisbeek, A. M. (2002) *J. Exp. Med.* **196,** 1–13.
52. Wyss, D. F., Choi, J. S., Li, J., Knoppers, M. H., Willis, K. J., Arulanandam, A. R. N., Smolyar, A., Reinherz, E. L. & Wagner, G. (1995) *Science* **269,** 1273–1278.